Orientation-Dependent Low Field Magnetic Anomalies and Room-temperature Spintronic Material – Mn doped ZnO films by Aerosol Spray Pyrolysis

S.S Nkosi, I. Kortidis, D.E. Motaung, G.F. Malgas, J. Keartland, E. Sideras-Haddad, A. Forbes, B.W. Mwakikunga, S. Sinha-Ray, G. Kiriakidis

PII: S0925-8388(13)01488-6
DOI: http://dx.doi.org/10.1016/j.jallcom.2013.06.090
Reference: JALCOM 28823

To appear in:

Received Date: 10 January 2013
Revised Date: 20 March 2013
Accepted Date: 15 June 2013

Please cite this article as: S.S Nkosi, I. Kortidis, D.E. Motaung, G.F. Malgas, J. Keartland, E. Sideras-Haddad, A. Forbes, B.W. Mwakikunga, S. Sinha-Ray, G. Kiriakidis, Orientation-Dependent Low Field Magnetic Anomalies and Room-temperature Spintronic Material – Mn doped ZnO films by Aerosol Spray Pyrolysis, (2013), doi: http://dx.doi.org/10.1016/j.jallcom.2013.06.090

Orientation-Dependent Low Field Magnetic Anomalies and Room-temperature Spintronic Material – Mn doped ZnO films by Aerosol Spray Pyrolysis

S.S Nkosi[1,2], I. Kortidis[4], D.E. Motaung[3,*], G.F. Malgas[3], J. Keartland[2], E. Sideras-Haddad[2], A. Forbes[1,2], B.W. Mwakikunga[3,†], S. Sinha-Ray[3], G. Kiriakidis[4]

[1]CSIR-National Laser Centre, 626 Meiring Naude Rd, Brummeria, Pretoria 0001

[2]School of Physics, University of Witwatersrand, Private Bag X3, Johannesburg 2030

[3]DST/CSIR Nanotechnology Innovation Centre, National Centre for Nano-Structured Materials, Council for Scientific and Industrial Research, P.O. Box 395, Pretoria, 0001, South Africa

[4]Institute of Electronic Structure and Laser, Foundation for Research and Technology, Hellas, P.O. Box 1527, 71110 Heraklion, Crete, Greece

ABSTRACT

High quality un-doped and Mn-doped ZnO films deposited by a simple aerosol spray pyrolysis technique for 20 and 30 minutes were studied using electron paramagnetic resonance (EPR), X-ray diffraction (XRD) and atomic force microscopy (AFM) techniques. EPR analysis showed novel observation of low field microwave absorption (LFMA) on the manganese (Mn) doped zinc oxide (ZnO) films at various Mn concentrations. The results showed a peculiar behaviour, reversal signal to that of LFMA. These findings also demonstrated that these films contain ferromagnetism at room temperature with possible applications in spintronics. Angular dependence measurements were found to induce magnetic transition from ferromagnetism to

* Corresponding Author: Dr. David Motaung, Tel: (+27) 12 841 4775,
Fax: (+27) 12 841 2229, Email: dmotaung@csir.co.za
† Corresponding Author: Dr. Bonex Mwakikunga, Tel: (+27) 12 841 4771,
Fax: (+27) 12 841 2229, Email: bmwakikunga@csir.co.za

paramagnetism. Structural analysis showed that the undertaken materials are in wurtzite structures. The light absorption edge of Mn-ZnO films red shifted which enhanced the observed ferromagnetism. The direct modulation of the band gap caused by Mn-ZnO substitution is responsible for the red shift effect in absorption edge of ZnO.

Keywords: Spray pyrolysis; Zinc oxide; Spintronics; Low-field microwave absorption; Magnetic transition

1. INTRODUCTION

Materials with novel combinations of properties such as room temperature ferromagnetism and semi-conductive properties are required for spintronic devices. Diluted magnetic semiconductors (DMSs) have attracted intense interest due to their potential applications in spintronic devices which utilize both the charge and spin of electrons to create new functionalities beyond conventional semiconductors **[1-3]**. DMSs are semiconductor solid solutions, where a small percentage of cations are replaced by magnetic impurities such as Mn. Due to the host sp-Mn d interactions in these DMSs, ferromagnetism can be produced **[3, 4]**. The main challenge for this kind of novel materials is to preserve their magnetic character at room temperature and above in order to be useful for technological applications. According to the ferromagnetic exchange coupling theory, an ideal DMS should have a homogeneous distribution of the magnetic dopants. The presence of any magnetic precipitate in the host semiconductors in the form of secondary phases of the magnetic impurities is detrimental to the real applications of DMSs and therefore should be avoided **[5]**. In the exploration of the specific materials, zinc oxide (ZnO) has been identified as an

excellent candidate host semiconductor for supporting room-temperature ferromagnetism when doped with a variety of 3d transition metal ions, particularly Mn^{2+} **[6]**. Room-temperature ferromagnetism for Mn doped ZnO was first reported by Sharma et al. **[7, 8]**, even though this DMS was specifically highlighted in theoretical studies for its high-T_c (Curie temperature) ferromagnetism potential **[6]**. Futhermore, ferromagnetism above room-temperature were reported for ZnO doped with cobalt (Co) **[9]**, iron (Fe) **[10]** and vanadium (V) **[11]** by using pulsed laser deposition (PLD).

This led to the study of p-conducting group III-V and group II-VI diluted magnetic semiconductors due to their wide band gap energies as prospective DMSs for achieving magnetic ordering at ambient temperatures and above. For example, a Curie temperature above room-temperature, 940 K, has been reported for p-conducting (Ga, Mn)N **[12]**. Since metallic manganese (Mn) is paramagnetic, any ferromagnetism detected in Mn doped ZnO cannot be due to Mn clusters formed during the growth process. Ferromagnetism near or above room temperature has already been reported for Mn-doped ZnO nanocrystals, pellets and thin films **[7, 13-14]**, whereas in other studies only paramagnetic behaviour was reported **[15-17]** among others. However, in all these previous works, it has been difficult to implement homogeneous doping through various fabrication approaches. In the same area of ferromagnetism, a relatively new phenomenon called “low-field microwave absorption” has been observed in ferromagnetic materials and other various materials such as high temperature superconductors, ferrites, manganites, doped silicate glasses and soft magnetic materials. Different interpretations have been put forward to try and explain this phenomenon. Paramagnetic defects in an

un-doped ZnO were also observed on EPR system by Xu et al. **[18]** which they claimed to cause ferromagnetism.

In this study an aerosol spray pyrolysis technique for the preparation of metal oxide nano-materials was used, due to its advantages of implementation of doping at the same time of metrical crystal growth process. This technique has been used to produce good ZnO nanostructures for photocatalytic and gas sensing application **[19-21]**. Therefore, in this article we report on the observation of ferromagnetism of Mn doped ZnO films grown by aerosol spray pyrolysis at various Mn atomic percentages and deposition times (20 and 30 min). More interestingly, an observation of low-field magnetic anomalies is reported. Room temperature ferromagnestism was observed which is directly affected by the addition of Mn in ZnO matrix. Furthermore, angular dependence of the ferromagnetism of Mn doped ZnO films together with the low-field magnetic anomalies are also studied. The structural, surface morphology and optical properties of un-doped and Mn doped ZnO DMS materials are also investigated in detail.

2. EXPERIMENTAL DETAILS

2.1 Synthesis of un-doped and Mn doped ZnO films grown by aerosol spray pyrolysis

The un-doped and Mn doped ZnO films were fabricated in a home-made aerosol spray pyrolysis system **[20, 21]**. The spray solution was prepared by dissolving appropriate volumes of solution containing 0.1 M zinc nitrate dehydrate $Zn(NO_3)^2$ (purity > 99%, Sigma-Aldrich) and different dopant concentrations of Mn

(0.1 - 5 at.%) in distilled water. The solutions were stirred at room temperature for a few minutes to yield a clear and homogeneous solution. The films were deposited at a constant flow rate of 300 ml h^{-1} by means of a nozzle assisted by a nitrogen carrier gas at 0.5 bar, over a heated corning glass substrate. The distance between the tip of the nozzle and the substrate was kept at 28 cm. The un-doped and Mn doped ZnO films were deposited for 20 and 30 min at a substrate temperature of 350 ˚C. Temperature of the heating plate and substrate was recorded by a K-type thermocouple and controlled by a Eurotherm400 temperature controller. All the films have been prepared by varying the Mn concentration. Prior to deposition, corning 1737 F glass substrates (25.4×25.4 mm^2) were ultrasonically cleaned with acetone, ethanol and deionized water.

2.2 Characterization

To study the structural properties of the pure ZnO and Mn doped ZnO films, X-ray diffraction (XRD) patterns were recorded on a Phillips (PANalytical X' pert PRO PW 3040/60) X-ray diffractometer using a Cu Kα (λ = 0.154 nm) radiation source. The measurements were recorded at 45.0 kV and 40.0 mA. Data were obtained from 2θ = 25 to 90˚. To study the cross-sectional view of the ZnO films, focused ion beam scanning electron microscopy (FIB- SEM, Auriga) was performed by means of ion-beam milling. Descriptions of how the focused ion beam (FIB) is used to prepare cross sections and transmission electron microscopy (TEM) specimens can be found elsewhere **[22-24]**. For cross-sectional analysis, a JEOL-2100 HR-TEM, operated at 200 kV was used. Atomic force microscopy (AFM) topography images of the films were analysed using a Veeco AFM system (Digital Instruments) in tapping mode. The energy-dispersive X-ray spectroscopy (EDX) mapping analyses were carried out

using a scanning electron microscope (JEOL - JSM 7500 HR-SEM) operated at an accelerating voltage of 15 keV. To measure the film thicknesses (Fig. 4b), variable spectroscopic ellipsometry (VASE) measurements were performed using a J.A. Woollam M2000 ellipsometer. The microwave absorption measurements were carried out using JEOL electron spin resonance (ESR) spectrometer operated at 9.4 GHz (x-band). For the analysis, the films were mounted in the cavity centre at a position where the microwave magnetic field is the maximum. The DC static field H_{DC} was slowly swept between 0 and 500 mT. The microwave power was kept at 5 mW to avoid saturation. The DC field was modulated with a superposed ac field whose amplitude was varied between 1 mT and 6 mT at 100 kHz frequency. The microwave response was measured as a derivative of microwave absorption signal. It should be pointed out that the measurements were carried out at room temperature (298 K). The ultraviolet-visible (UV-vis) absorption spectra were carried out using a PerkinElmer Lambda 750 UV-vis spectrometer.

3. RESULTS AND DISCUSSION

Fig. 1 shows the X-ray diffraction (XRD) patterns for the un-doped and Mn doped ZnO films deposited for 20 and 30 min using the aerosol spray pyrolysis (ASP) method. All of the diffraction peaks can be indexed within the experimental error as hexagonal ZnO phase (wurtzite structure) with a lattice constant of *a* = 0.3249 and *c* = 0.5206 nm by comparison with the data from the Joint Committee on Powder Diffraction Standards (JCPDS) card for ZnO (JCPDS: 36-1451).

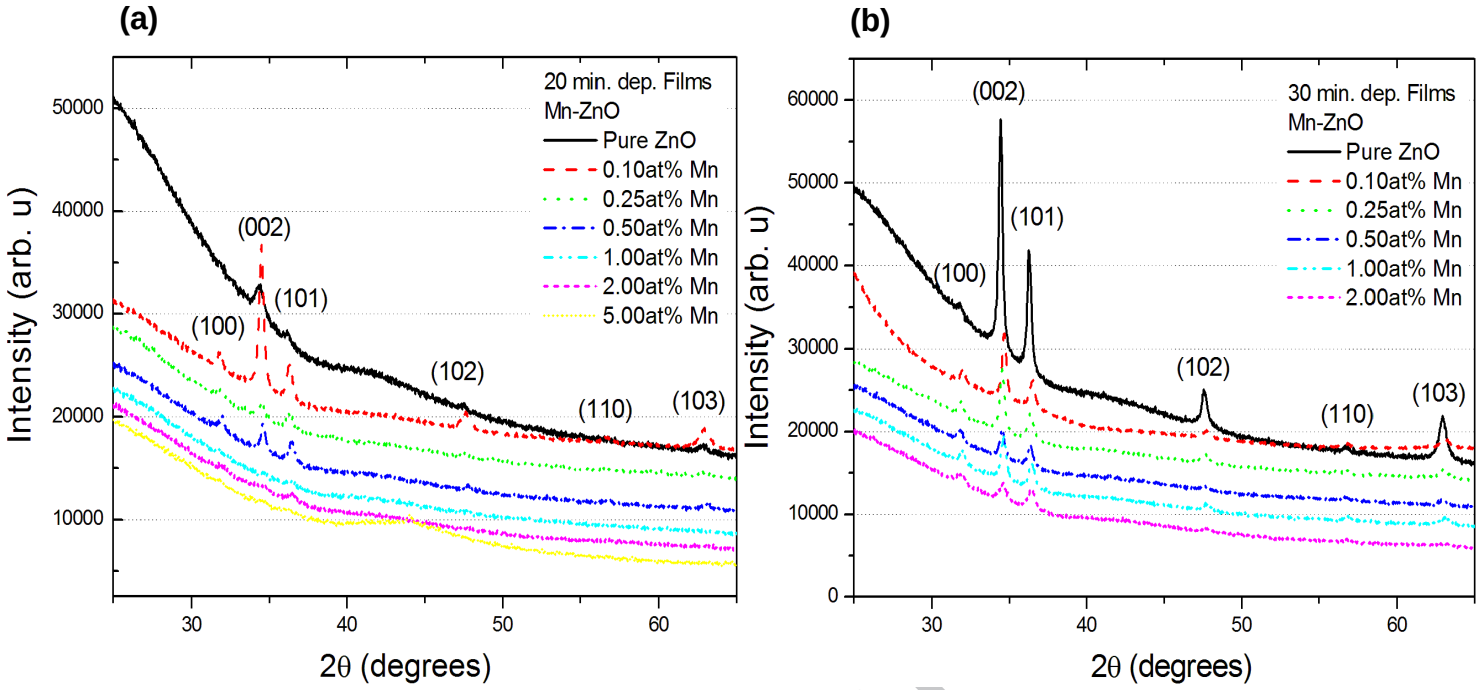

Fig. 1: XRD patterns of the Mn doped ZnO films deposited for (a) 20 and (b) 30 min.

No characteristic peaks from other impurities were detected for the un-doped ZnO films, indicating a high purity product. The sharper and strong peaks also confirm that the films are highly crystalline. It is further observed that the un-doped ZnO films exhibit a strong orientation along *c*-axis (002). Other orientations corresponding to (100) and (101) are present with low relative intensities. When the ZnO films are doped with a low Mn concentration, the diffraction peaks shift towards higher 2θ angles. This might be due to an incorporation of Mn ions into the host matrix as depicted in Table 1. Therefore, this signifies that the lattice parameter, *a,* increases while the lattice parameter *c* decreases with increasing Mn doping level, presumably resulting from the substitution of Mn^{2+} ions with a large ionic radius of 0.66 Å for Zn (0.60 Å) **[25]**. However, previously studies **[26-29]** showed that the diffraction peaks of the ZnO shift towards lower 2θ angles upon incorporating Mn ions into the ZnO matrix, resulting in an increase in both lattice parameters *a* and *c*.

The lattice parameters for hexagonal ZnO and Mn-doped ZnO films were estimated from the following equation:

$$\frac{1}{d_{hkl}^2} = \frac{4}{3}\frac{\left(h^2 + k^2 + hk\right)}{a^2} + \frac{l^2}{c^2} \quad (1)$$

where *a* and *c* are the lattice parameters and *h, k*, and *l* are the Miller indices and d_{hkl} is the inter-planer spacing for the plane (*hkl*). This inter-planer spacing can be calculated from Bragg's law equation **[30]**. At higher Mn concentration the intensity of the (002) orientation is suppressed for both films (20 and 30 min), indicating that the orientation of the ZnO along (002) has been disturbed after higher Mn doping. Therefore, at higher Mn doping level, the dopants will migrate from ordered substitutional sites within the lattice to more disordered regions, most likely the surface of the nano-crystals **[25]**. These results also demonstrate that there is an optimal doping level during the synthesis of Mn doped ZnO materials. The volume of the unit cell for the hexagonal system has been calculated from the following relation:

$$V = 0.866 \times a^2 \times c \quad (2)$$

It is observed from Table 1 that the volume of the unit cell decreases with an increase in Mn doping level up to 1 at.% of Mn. However at higher doping levels, an increase in the volume of the unit cell is observed. According to Vegard's Law **[31, 32]**, by incorporation of Mn ions into the ZnO lattice could easily be obtained from the lattice constants. To estimate the ZnO nanocrystallite sizes for the <002> orientation, the Debye-Scherrer formula was used **[30]**:

$$L_{hkl} = \frac{0.9\lambda}{B_{2\theta}\cos(\theta)} \quad (3)$$

where λ is the wavelength of the x-rays, $B_{2\theta}$ is the full width at half maximum intensity (FWHM) and θ is the diffraction angle. Table 1 shows that the ZnO crystallite sizes related to the (002) peak decreases with doping concentration of Mn.

Fig. 2 shows cross-sectional transmission electron microscopy analysis of the un-doped and 2at. % Mn doped films. It can clearly be seen from Fig 2a that the 20 min film composed of nanoparticles with an average size of 5.5 ± 0.5 nm. From high resolution TEM analysis it is observed that the thickness of the same film is approximately 42.5 nm. Selected area electron diffraction (SAED) pattern shows broad diffused Debye rings due to the small sizes of the ZnO nanoparticles. Indexing of the SAED (inset) pattern is attributed to (002), (100) and (102) peaks of the crystalline phase of ZnO nanoparticles. The 2 at.% Mn doped ZnO as depicted in Fig. 2b also shows diffused rings with few diffraction spots due to the Mn **[33]**.

Cross-sectional view of the 30 min deposited film (Fig. 2c) reveals that the columnar structures grow perpendicular to the substrate and has a parallel *c*-axis orientation. It is therefore believed that these columnar structures are induced by the formation of nanoparticles with increasing time **[34]** and their typical column size range from 20 to 60 nm, while the ZnO film thickness is around 170 nm. The HR-TEM micrograph (Fig. 2e) and the SAED patterns (inset) shows a clear lattice fringes with a *d*-spacing of 0.26 and 0.28 nm, which corresponds to the (002) and (100) lattice planes of hexagonal ZnO and confirms that the ZnO structures are polycrystalline in nature.

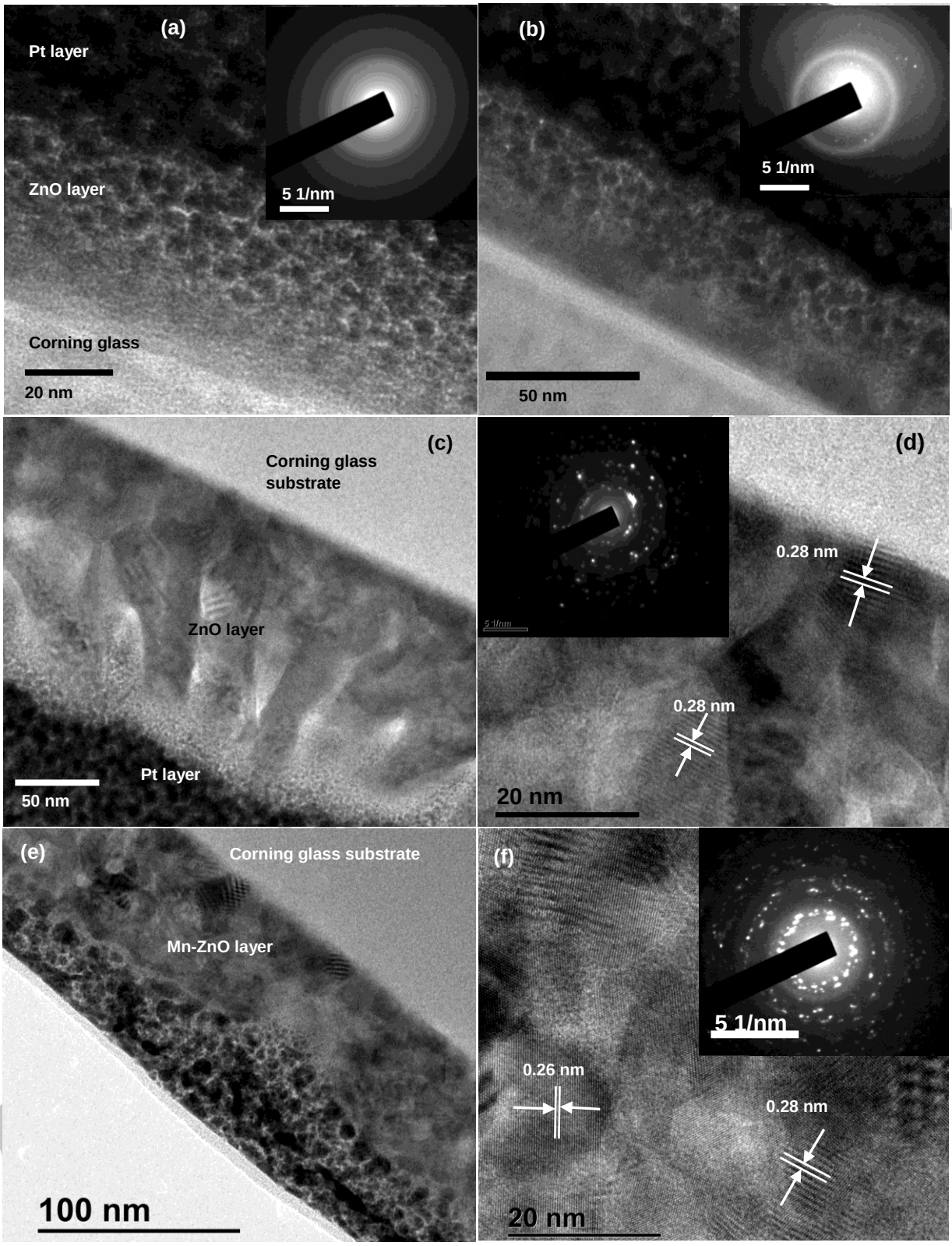

Fig. 2: HR-TEM micrographs of a cross sectional analyses of un-doped ZnO deposited for (a) 20 min, (b) 2 at. % Mn-doped 20 min film, (c-d) un-doped ZnO deposited for 30 min and (e-f) 2 at. % Mn-doped ZnO 30 min deposited film, and their corresponding SAED patterns.

It is observed from Fig. 2f that when 2 at.% Mn is doped in the ZnO matrix; the columnar structures are hardly observed across the film. However, the corresponding SAED pattern shown in the inset of Fig. 2f indicates that the polycrystalline behaviour is not completely hindered by incorporation of Mn in the ZnO host. **[33]**

Fig. 3 depicts the energy dispersive X-ray analysis (EDX) and the elemental mapping of the 2 at.% Mn doped ZnO film grown for 30 min. The line scan of EDX spectrum and the mapping (Figs. 3a–f) suggests a reasonably good homogeneity of elements (Zn, Mn, O) distribution (within the experimental error due to varying surface roughness). The silver and silicon present in the EDS spectrum are from the silver paste used as coating and glass substrate, respectively. More interestingly, the mapping of elements, as shown in Fig. 3d, indicated no appreciable clustering or segregation of Mn atoms in the ZnO matrix. This concludes that the doping of Mn into Zn sites of samples and also rules out any significant role of Mn clustering on the observed RTFM.

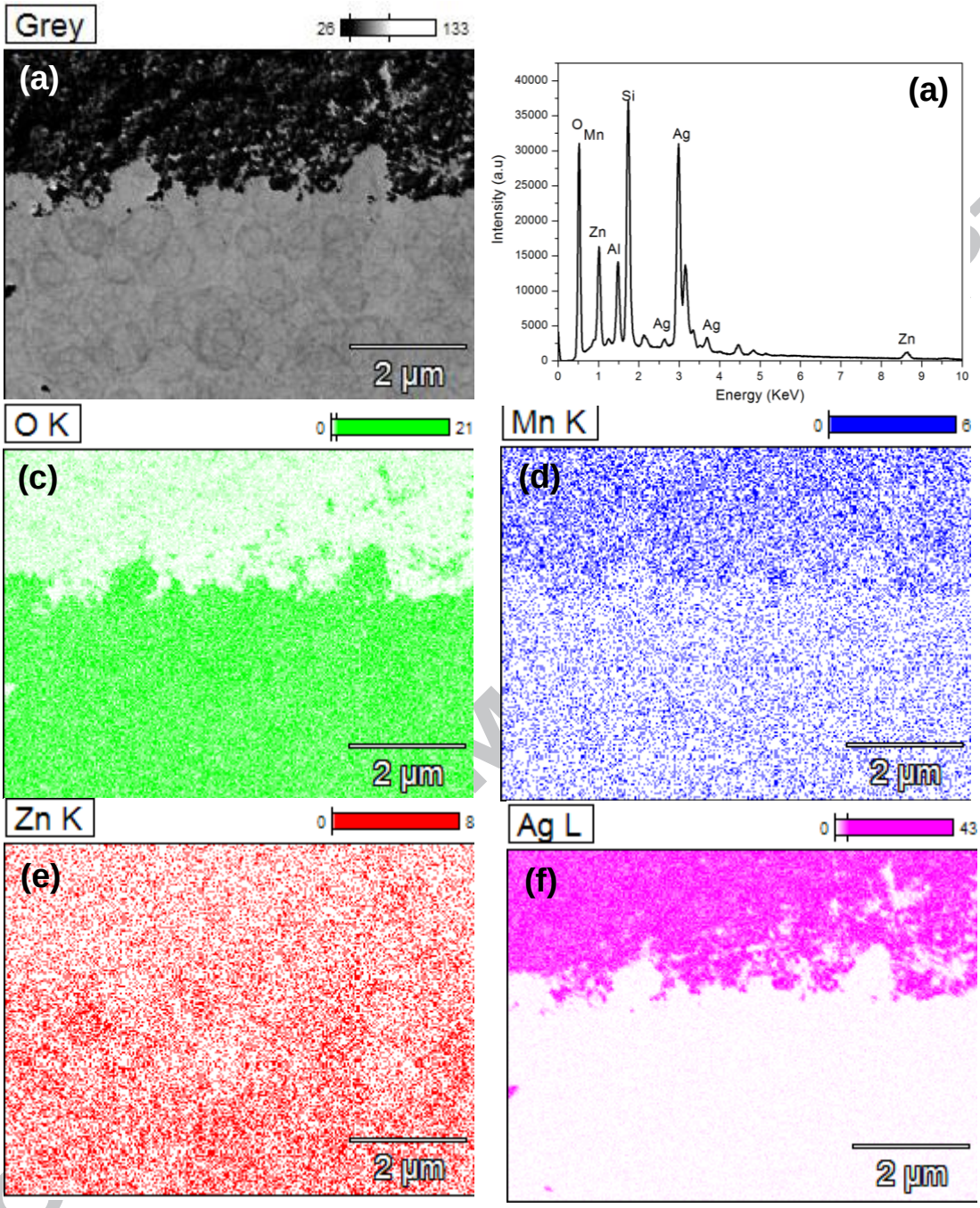

Fig. 3: EDX pattern with the composition of the elements. Elemental mapping of (c) O (d) Mn (e) Zn and (f) Ag taken from the area of the SEM as shown in (a). Elemental scan [O (green), Mn (blue), Zn (red) and Ag (purple)].

The surface microstructure studies of the un-doped and Mn doped ZnO films for different Mn concentrations have been studied by using atomic force microscopy

(AFM) and the results are displayed in Fig. 4. The un-doped ZnO film deposited for 20 min shows a well adherent and smooth film with small ZnO particles ranging from 5 to 10 nm. Upon introducing the 0.1 at.% of Mn in the ZnO, particles sizes related to ZnO increases (Fig. 4b). Increasing the Mn concentration (0.5 - 2 at. %), the surface morphology of the films deposited for 20 min films changes drastically, resulting to an increase in the particles size and the surface roughness. These changes in surface morphology might lead to degradation in the crystalline quality of the film. Fig. 4e shows the un-doped ZnO nanorods grown for 30 min by ASP. These ZnO nanorods are grown perpendicular to the substrate, entangled to one another forming “spaghetti-like” structures. These “spaghetti-like” structures with an average diameter in the range of 25-35 nm were previously observed by Motaung et al. **[34]**. When Mn ions are inserted in the host matrix, the particles/rods related to ZnO grow perpendicular to the substrate. At higher doping level the microstructure is dominated by large nanorods growing across the film.

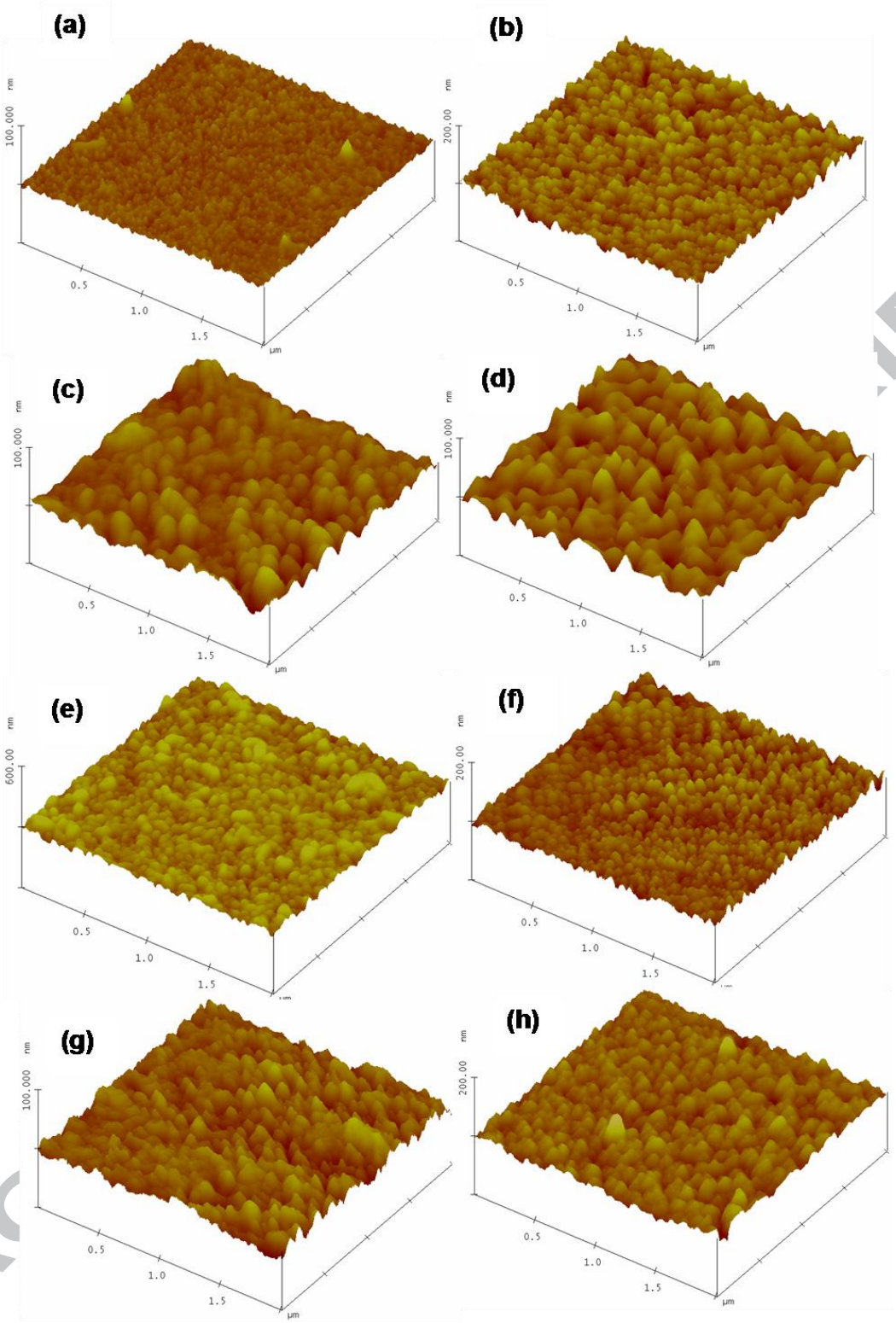

Fig. 4: AFM 3D images of (a) undoped ZnO grown for 20 min, (b-d) Mn doped ZnO films at 0.1, 0.5 and 2 at. % deposited for 20 min, (e) undoped ZnO grown for 30 min and (f-h) Mn doped ZnO films at 0.1, 0.5 and 2 at.% deposited for 30 min.

To quantitatively investigate the changes in the morphology, the surface roughness (rms) values for the Mn-ZnO films were measured as shown in Fig. 5. It is observed that both films deposited for 20 and 30 min show a different behaviour on the surface roughness with an increase in Mn doping concentration. The surface roughness of the films after a 20 min deposition time increases with an increase in the level of doping in the host matrix which is consistent with the film thickness shown in Fig. 5b. However, it is interesting to note that the surface roughness (Fig. 5a) as well as the film thicknesses (Fig. 5b) of the films deposited for 30 min decrease with an increase in Mn doping. The increase in the surface roughness and film thicknesses for the 20 min might be due to the fact that by incorporating Mn in the ZnO, resulted in an increase in the diameter of the grains/rods and valleys. While the decrease in the film surface roughness and thickness for the films deposited for 30 min is due to a limited growth in grains or rod-like structure formations. There is an observed interception point at around 0.75 at.% Mn indicating that at this doping level (0.75 at. %) the surface roughness (~ 2.6 nm) for both films is equivalent.

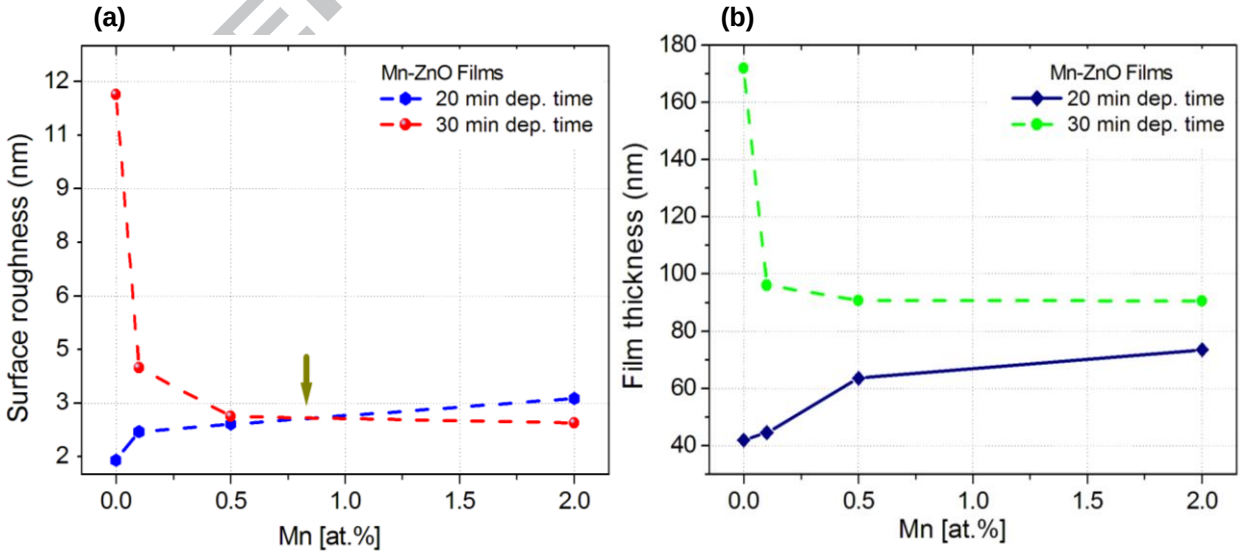

Fig. 5: Evolution of the (a) surface roughness and (b) film thickness as a function of Mn concentration.

The plots in Fig. 6 and 7 depict the derivative of microwave absorption as a function of magnetic flux density (DC field) for Mn doped ZnO films deposited for 20 and 30 min by an aerosol spray pyrolysis (ASP) technique, respectively. The measurements were taken at room-temperature (T=298 K) at a microwave power of 5 mW. The dependence of the in-plane and out-of-plane microwave absorption is also shown. The plots exhibit three absorption peaks associated with three processes; centred at $H_{DC} \approx 6.0$ mT, 150 mT and 300 mT which are assigned to low field signal, paramagnetism and ferromagnetic resonant field, respectively. Ferromagnetic resonance (FMR) is due to the absorption in the full saturation state. The low field microwave absorption (LFMA) process usually originates from the magnetization process far from the saturation state. These results confirm the appearance of FMR at room-temperature. Moreover, the observations of the low field magnetic signals are novel in this present work. LFMA is understood to be connected to the magnetization processes that occur at low field densities. We therefore assume that the magnetization is present at relatively low magnetic field. Such magnetization process is attributed to the interaction of magnetic moments of the Mn-ZnO films deposited for 20 and 30 min with the magnetic field component of electromagnetic radiation. These low field observations are studied with the variation of Mn concentration.

Fig. 6a shows an EPR spectrum for un-doped and Mn doped ZnO films synthesized by ASP for 20 min. For these analyses the DC field was kept parallel to the films. It is observed that when the dopant concentration is increase from a low (0.1 at% Mn) to high (5.00 at% Mn) atomic percentage of Mn; that both ferromagnetism and a paramagnetic feature at ~ 150 mT are present in all dopants.

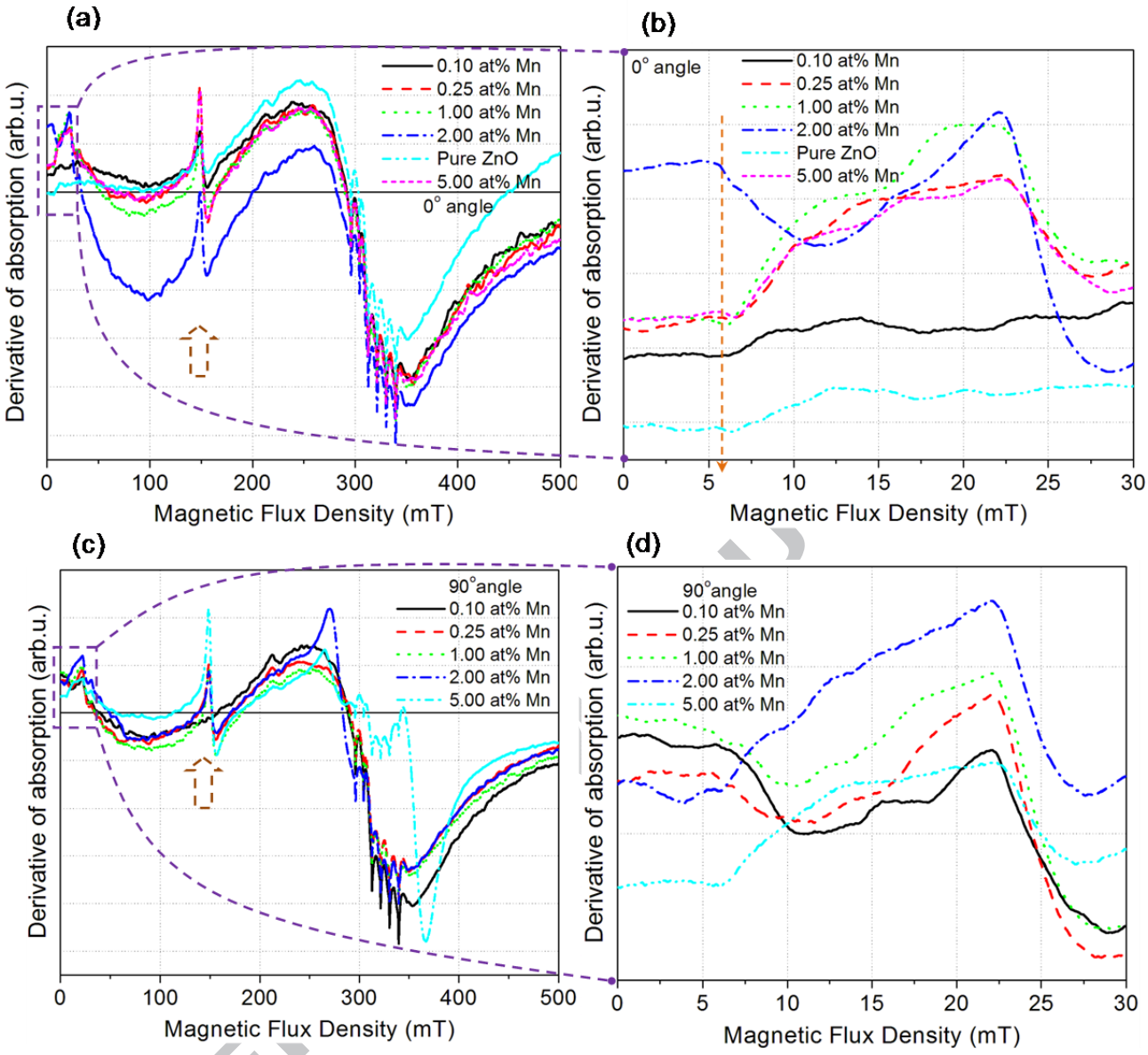

Fig. 6: EPR measurement for the undoped and Mn doped ZnO films deposited for 20 min. The film geometry was always kept parallel to the magnetic field and (b) corresponds to the zoom-in at low field (~ 6mT).

These films induce hyperfine structures known to be from an electron and Mn-Zn nucleus interaction. They have high intensities due to the angular momentum of a density of free unpaired electrons. ZnO is well known as a semiconducting material with some free unpaired electrons contributing to high angular momentum around

the nucleus. Our previous EPR analyses revealed that nickel oxide and iron-platinum particles contain anomalous hyperfine structures **[35-36]**. By varying the doping level of Mn, the low magnetic field signals are studied in detail. It is observed that the pure ZnO together with a 0.1 at% Mn does not show any significant change in the electromagnetic radiation (microwave) at the low-fields, hence no microwave absorption could be detected. However, increasing the Mn dopant levels up to 5.00 at%, microwave absorptions at relatively low field of about 6 mT are observed. In contrast, a dopant concentration of 2.0 at% Mn in the host matrix resulted in strange behaviour or rather an emission at the same low field. This unusual behaviour is not yet fully understood to whether it is an emission or absorption from opposite spins, since it is opposite to the earlier LFMA signals obtained from the different Mn dopants. Additionally, if it is called an emission, then it is also not clear whether it is a microwave emission or another form of electromagnetic radiation i.e. radio waves, etc. Since ZnO semiconductor has a wide band gap of ~ 3.3 eV, it is not expected that any energy from microwave to excite an electron from the lower state up to the higher state to induce emission. Shinde et al. **[37]** showed that when ZnO is doped with a transition metal like Mn^{2+} ; its band gap reduces allowing a transition to occur, hence a low energy emission i.e. microwave or radio-waves to take place. Or another form of defect related emission can occur which we are likely to believe is from a low-energetic centre. First of all, the fact that the un-doped ZnO film shows magnetization features constitutes the most puzzling question concerning DMSs. Recent studies reported that although a single isolate oxygen vacancy cannot have a magnetic moment, a cluster of such vacancies may very likely carry a net moment **[18, 38]**. When these clusters interact with each other, i.e. either directly or indirectly through isolated oxygen vacancies, it is possible that magnetic ordering occurs,

which may lead to a magnetization. Furthermore, it is well known that oxygen vacancies may easily be formed in ZnO and that the lowering of grain size distribution may increase interface defects **[39, 40]**.

In addition, an angular dependence of these films Mn-ZnO was performed by tilting or measuring the films perpendicular to the applied magnetic field. Fig. 6c shows the derivative of the absorption spectra for the Mn doped ZnO films. It is worthy to point out that a peculiar behaviour is observed at the low atomic (0.1 at% Mn) percentage thin film. The film does not contain any paramagnetic feature at 150 mT. However, the 0.25 and 1.0 at% of Mn thin films contain ferromagnetism with the paramagnetic feature at 150 mT. The fact that this paramagnetic feature appears at the same field is a clear indication that these are from the same clusters attributed to Mn and are angular independence at higher Mn concentration. Moreover, magnetic transition is observed from 2.0 to 5.0 at% of Mn thin films of ZnO when the films are tilted (or measured at) 90 °. The signal related to ferromagnetism transform to a sharper peak at 2.0 at% Mn related to paramagnetism. A similar transition has been observed by Nkosi et al. **[35]** for nickel oxide at room temperature induced by substrate annealing. Upon increasing the doping level of Mn, the ferromagnetism completely disappears to another form of magnetism related to paramagnetic. The spins become randomly orientated at higher atomic percentages of Mn. Based on above analysis we believe that such high Mn doping level in ZnO materials should not be developed for spintronic devices.

Angular dependence of low-field absorption on the mutual orientation DC static field magnetic field H_{DC} and the films surface also help us to further study the role of anisotropy on the low-field signal. Fig. 6d shows the EPR analysis of the Mn doped

ZnO films (deposited for 20 min) measured perpendicular to the H_{DC} field for low magnetic field. It is worthy to point out that the low doping levels of (0.1, 0.25 and 1.0 at% Mn) Mn shows an emission whereas the high Mn concentrated ZnO films show microwave absorption. Almost all the Mn-ZnO thin films measured at angle of 90˚ except the 5.0 at% Mn are showing opposite signals when compared to the thin films measured parallel (0˚) to the H_{DC} field. This indicates that the film with higher Mn concentration is angular independent at low field while the 0.1 at% Mn film showed LFMA at 90˚. When the film was measured at 0˚ no signal related to absorption or emission was observed.

Fig. 7a shows an EPR spectrum for the 30 min deposited film measured parallel to the magnetic field. No paramagnetic feature appeared at 150 mT for the 0.1 at% Mn film. However, ferromagnetism is observed for films doped with 0.1, 0.25 and 1.00 at% of Mn. Upon increasing the Mn concentration, a magnetic transition occurs. This magnetic transition signal is not the same as that observed in the films deposited for 20 min at an angle of 90˚, where the signal related to ferromagnetism transform to a sharper peak at 2.0 at% Mn related to paramagnetism. Therefore, the 30 min films seem to be dominated by the same spins which are randomly oriented clusters with some ferromagnetic features still present even at relatively high Mn concentration.

Fig. 7b shows low field microwave absorption spectrum for the films (deposited for 30 min) measured parallel to the H_{DC} field. All the films show low-field microwave absorption except at higher Mn concentration (5.00 at% Mn); which shows relatively low emission compared to its counterpart. However, when the films are measured perpendicular to the H_{DC} field, the paramagnetic feature at 150 mT appears. This feature at 150 mT was not observed when the films were measured parallel to the

magnetic field (Fig. 7c). It should be pointed out that all the films deposited for 30 min contain ferromagnetism even at higher Mn concentration. It is worthy to note that this kind of behaviour was not observed for 20 min films at the same angle.

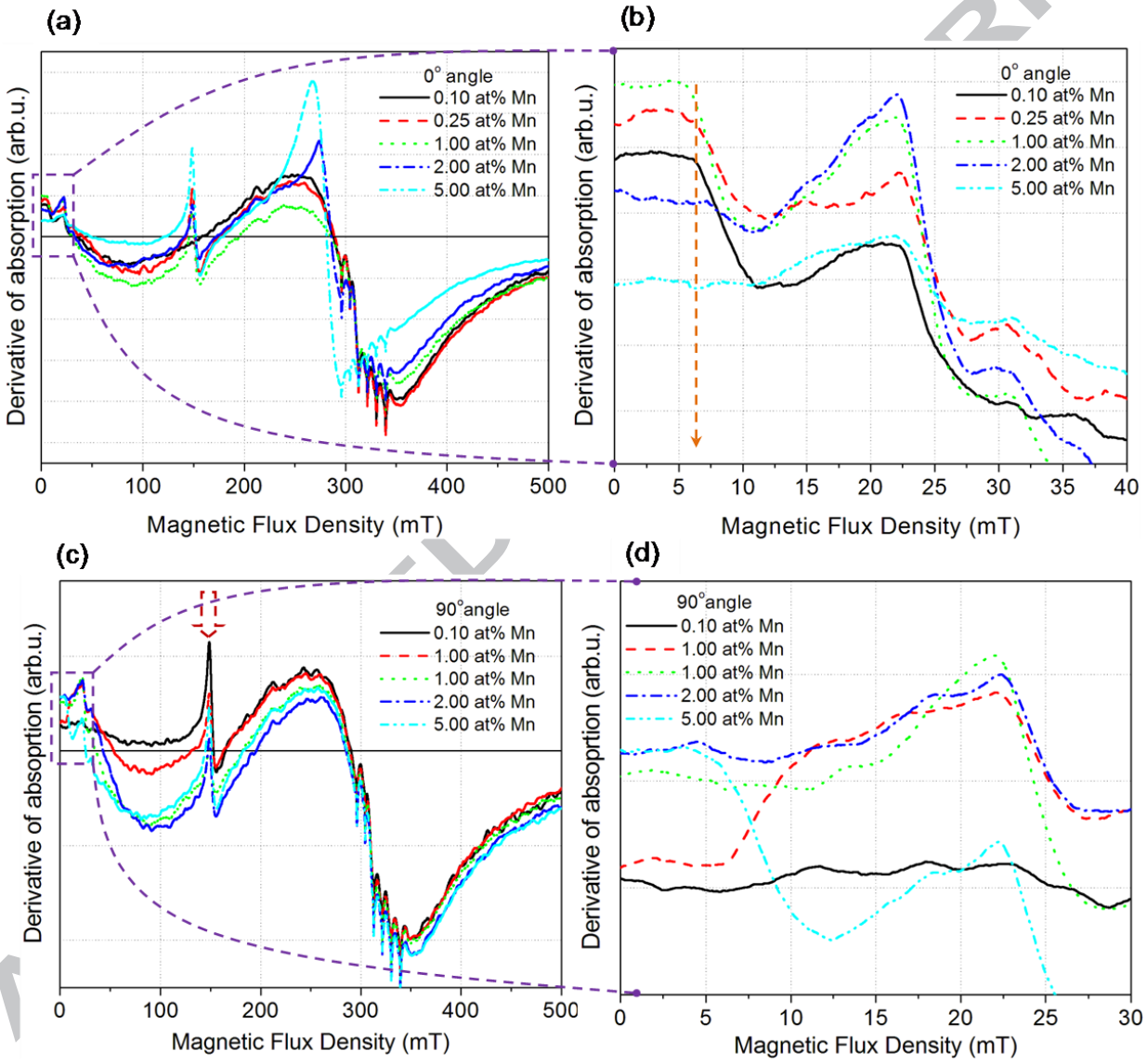

Fig. 7: EPR measurement for the undoped and Mn doped ZnO films deposited for 30 min. The film geometry was always kept parallel to the magnetic field and (b) corresponds to the zoom-in at low field (~ 6mT).

The angular dependence of the low-field for the films deposited for 30 min,was studied by tilting the films at an angle of 90˚ to the magnetic field, H_{DC} as shown in Fig. 7d. At a low doping level (0.1 at% of Mn), the film does not show any signal related to low-field. By increasing the doping level to 0.25, 1.00 and 2.00 at% of Mn, the films show low-field "emission" with 0.25 at% Mn relatively higher than 1.00 and 2.00 at% Mn, respectively. By further increasing the atomic percentage of Mn, low-field absorption is still maintained. This low-field microwave absorption phenomenon has been observed in ferromagnetic materials and various other materials such as superconductors, ferrites, manganites, semiconductors, doped silicate glasses, in soft materials and recently in iron monosilicides films **[41- 46]**. However, the new phenomenon observed in Fig. 6 and 7 which we call "low-field radiation emission" since it is opposite to LFMA has not been seen elsewhere in any other materials before. For this so called "low-field radiation emission" more work is required to explain it in detail.

For magnets and ferrites the LFMA signal is associated with the onset of the ordered phase and provides a sensitive detector of magnetic ordering **[42, 47]**. For high-temperature superconductors LFMA signal reveals a change to superconductive state **[41]**. In semi-conductors the LFMA signal is due to magneto-resistive effects **[47]**. For doped silicate glasses LFMA signal is due to magneto-induced microwave conductivity in the dielectric glass, which derives from spin-dependent charge migration within the first co-ordination of paramagnetic ions **[48]**. For soft magnetic materials the LFMA signal is due to low-field spin magnetization processes **[43, 49]**. Already researchers have found strong correlation between this LFMA and giant magneto impedance (GMI) phenomenon. Using complex Ponyting

vector, a correlation between LFMA and magneto impedance (MI) have been shown theoretically as given by the following equation:

$$\frac{dP_S}{dH} \alpha \frac{dR_e(Z_S)}{dH} \quad (4)$$

where this equation basically means that there is observable rate of change of electromagnetic radiation power (in this case microwave) at different magnetic field and that rate is directly proportional to the rate at which only the real part of impedance changes at those different magnetic field. This equation shows how the impedance evolves at different magnetic field for the LFMA phenomenon. Based on Eq. 4, the real part of impedance signal follows the microwave derivative signal at LFMA. Moreover, its signal can be intense than the microwave derivative signal depending on the nature of the constant used multiplying the impedance. Harth et al. **[50]** and Arizumi et al. **[51]** showed that it is possible to observe microwave emission from n-InSb at 77 K in the presence of magnetic and low electric fields. Harth et al **[50]** claimed that magneto-resistance effect and Doppler-shifted acoustic cyclotron resonance were proposed to be essential mechanisms which determine the magnetic dependence of the microwave emission. On other hand, Arizumi et al. **[51]** found close correlation between the microwave emission and acoustoelectric effect. Hence, concluding that the microwave emission from n-InSb at low-field is due to build-up of phonons caused by piezoelectrical coupling. While Lax et al. **[52]** published a paper in 1961 before Harth, Arizumi and co-workers about cyclotron resonance in Indium Antimonide at high magnetic fields. A paper of microwave emission from InSb from low electric fields was also published in 1966 **[53],** albeit a little can be learnt from these papers to fit our observation. The ferromagnetic feature

has a relatively hard and easy magnetization and low residual magnetization. This is attributed to the shape anisotropy effect **[54]**, which forces the magnetic moments to mostly align along the axis of the Mn-ZnO structures.

Fig. 8 shows the variation of ΔH_{PP}, FMR line width (mT), with Mn concentration for the Mn-ZnO films deposited for 20 and 30 min. The DC static magnetic field was parallel (0˚) to the films surface. The FMR line width showed a significant difference with Mn doping for both the 20 and 30 min films with respect to the XRD unit cell. The line width at lower Mn doping level increases while the volume of unit cell decreases (Table 1). However, at higher Mn doping, the line width decreases linearly with Mn concentration especially for the films deposited for 30 min, due to an exchange narrowing of the EPR signal. The substitution of Mn^{2+} sites supplements the XRD data where an increase in unit cell volume is observed for Mn^{2+} ion substituted sample. Therefore, this shows that the incorporation of Mn in the ZnO matrix has a major contribution to the change in the line width more especially for the 30 min deposited films. This is consistent with the AFM and Ellipsometry results where both surface roughness and film thickness decrease significantly with Mn content. This is also shows a clear indication of the magnetic transition observed at higher Mn concentration. Moreover, as stated above as the Mn concentration is increased, the resonance signal becomes broader and therefore the numbers of spins are increased (results not shown).

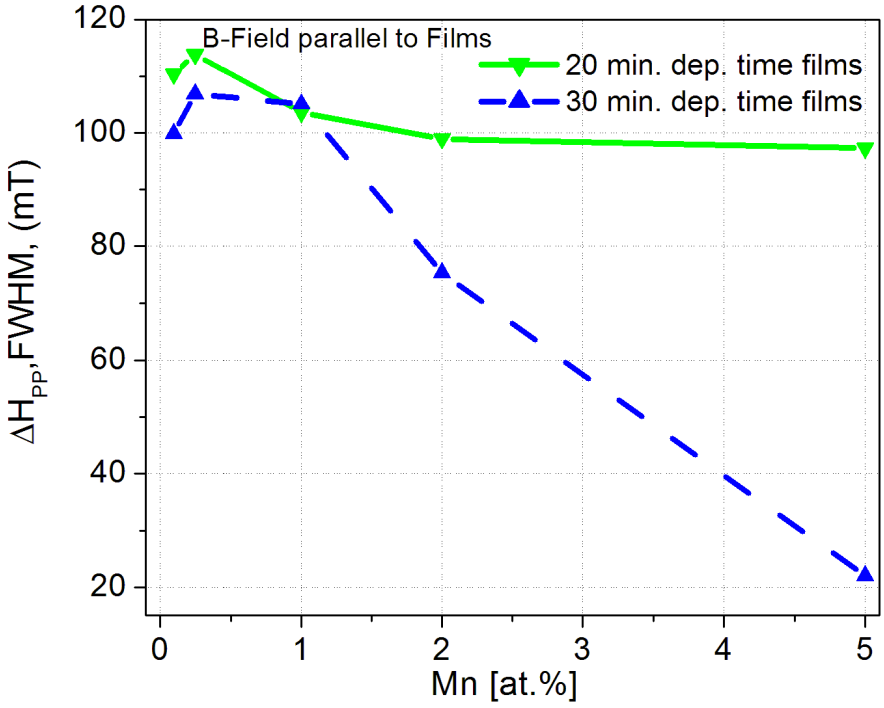

Fig. 8: The ΔH_{PP} dependence of FMR microwave absorption with Mn concentration measured parallel (0˚) to the magnetic flux density field for both 20 and 30 min deposited films.

As concentration increases, the number of spins could increase due to an increase in the absorption as observed in Fig. 9. It is noticed that the un-doped films show lower absorbance in the visible range of the spectrum. All of these samples exhibit a sharp absorption edge at about 370 nm. When Mn ions are inserted in the host matrix, an improved absorption is observed for both 20 and 30 min films. The rise in absorption, observed on dopant concentration, can be, thus, largely attributed to the observed decrease in crystallinity of the material as confirmed by the x-ray diffraction analysis, Fig. 1. Furthermore, it is observed that the absorption edge of the Mn doped ZnO films shows different behaviour. The absorption peaks for the films deposited for 20 min are red shifted. This red shift might be due to a reduced quantum confinement effect, while opposite occurs for the films deposited for 30 min. This is consistent with the opposite type of behaviour noticed on the AFM results

(Fig. 4). This red shift is in good agreement with the results reported by Shinde et al. **[37]**. This is due to the fact that absorption of higher energy photons causes activation of 'spd' exchange interactions and typical 'dd' transitions, which lead to the enhancement of ferromagnetic properties. So, similar activations may be expected here for spray deposited Mn-ZnO films. However, a blue shifted band gap of Mn doped ZnO films have shown no evidence of ferromagnetism deposited by other techniques on different substrate, epitaxially **[55]**. Moreover, it is evident that at higher Mn content in the host matrix, the absorption spectra of both 20 and 30 min films decrease. Furthermore, there is an absorption rim at around 320-330 nm that is shown by an arrow in Fig. 9a and b. It is only visible at lower Mn concentration and fading away at higher Mn concentration. This is probably due to some structural defect in crystal or strain present at the surface of the ZnO.

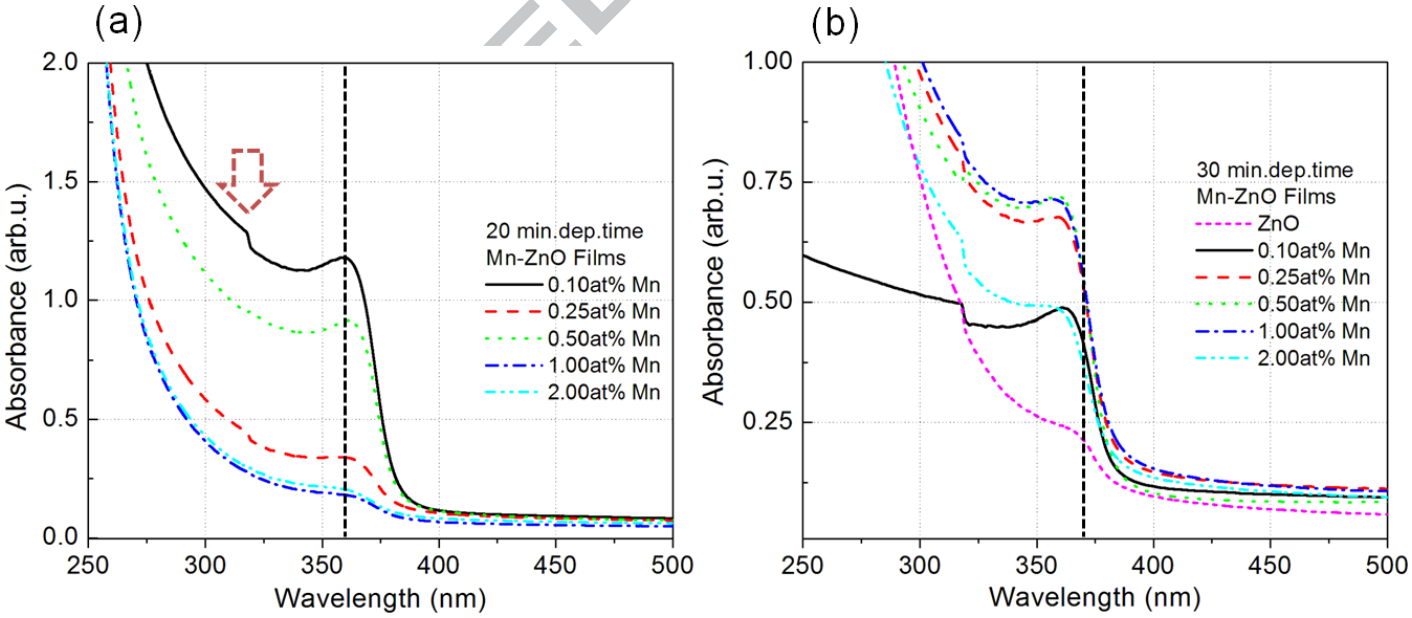

Fig. 9: UV-VIS absorption spectra of the undoped and Mn doped ZnO films deposited for (a) 20 min (b) 30 min.

4. CONCLUSION

Optimized un-doped and Mn-doped ZnO films with different dopant concentrations were grown on corning glass substrates by ASP technique. In these findings the low field microwave absorption (LFMA) was observed for the first time on the Mn-ZnO films deposited for 20 and 30 min. Moreover, some phenomenon which is completely opposite to that of LFMA signal, which is related to “low field microwave emission” was also observed for the first time in this work. A Mn addition to the ZnO films results in a red shift and an enhancement of the ferromagnetism. The structural analysis showed that the (002) orientations are suppressed by the addition of Mn and that the Mn^{2+} ions partially substitute Zn^{2+} sites. A more detail analysis on these magnetic anomalies will form part of our outlook in our laboratory.

5. ACKNOWLEDGEMENTS

This work was supported by the Department of Science and Technology, Council for Scientific and Industrial Research (HGER28P, HGER27S and LHIE100), WIROX project (PIRSES-GA-2011-295216), a Marie Curie International Research Staff Exchange Scheme Fellowship within the 7^{th} European Community Framework Programme and ‘ORAMA’ Oxide Materials Towards a Matured Post-silicon Electronics ERA FP7-NMP - CONTRACT N°: 246334. The authors are also thankful to Mr. Thomas Malwela, Dr. James Wesley-Smith and Ms Tutuzwa Xuma for FIB-SEM and HR-TEM analysis.

6. REFERENCES

[1] X.Y. Mao, W. Zhong, Y.W. Du, J. Magnetism and Magnetic Materials 320 (2008) 1102.

[2] I. Zutic, J. Fabian, S.D. Sama, Reviews of Modern Physics 76 (2004) 323.

[3] C. Jing, Y. Jiang, W. Bai, J. Chu, A. Liu, J. Magnetism and Magnetic Materials 322 (2010) 2395.

[4] E. Chikoidze, Y. Dumont, H.J. Bardeleben, W. Pacuski, O. Gorochov, Superlattices and Microstructures 42 (1-6) (2007) 176.

[5] R.Q. Wu, G.W. Peng, L. Liu, Y.P. Feng, Z.G. Huang, Q.Y. Wu, , Appl. Phys. Lett. 89 (2006) 062505.

[6] T. Dietl, H. Ohno, F. Matsukura, J. Cibert, D. Ferrand, Science 287 (2000) 1019.

[7] P. Sharma, A. Gupta, K.V. Rao, F.J. Owens, R. Sharma, R. Ahuja, J.M.O. Guillen, B. Johansson, G.A. Gehring, Nature Materials 2 (2003) 673.

[8] P. Sharma, A. Gupta, F.J. Owens, A. Inoue, K.V. Rao, J. Magnetism and Magnetic Materials 282 (2004) 115.

[9] K. Ueda, H. Tabata, T. Kawai, Appl. Phys. Lett. 79 (7) (2001) 988.

[10] Y.Q. Wang, S.L. Yuan, L. Liu, P. Li, X.X. Lan, Z.M. Tian, J.H. He, S.Y. Yin, J. Magnetism and Magnetic Materials 320 (2008) 1423.

[11] H. Saeki, H. Tabata, T. Kawai, Solid State Communications 120 (11) (2001) 439.

[12] H. Hori, S. Sonoda, T. Sasaki, Y. Yamamoto, S. Shimizu, Ken-inchi Suga, K. Kindo, Physica B 324 (2002) 142.

[13] D.P. Norton, S.J. Pearton, A.F. Hebard, N. Theodoropoulou, L.A. Boatner, R. G. Wilson, Appl. Phys. Lett. 82 (2003) 239.

[14] K.R. Kittilstved, N.S. Norberg, D.R. Gamlin, Phys. Rev. Lett. 94 (2005) 147209.

[15] S.S. Kim, J.H. Moon, B.-T. Lee, Oh S. Song, J Ho Je, J. Appl. Phys. 95 (2004) 454.

[16] T. Fukumura, Z. Jin, M. Kawasaki, T. Shono, T. Hasegawa, S Koshihara, H. Koinuma, Appl. Phys. Lett. 78 (2001) 958.

[17] A. Tiwari, C. Jin, A. Kvit, D. Kumar, J.F. Muth, J. Narayan, Solid State Communications 121 (2002) 371.

[18] X. Xu, C. Xu, J. Dai, J. Hu, Fengji Li, S. Zhang, J. Physical Chemistry C 116 (2012) 8813.

[19] G. Kenanakis, Z. Giannakoudakis, D. Vernardou, C. Savvakis, N. Katsarakis, Catalysis Today 151 (2010) 34.

[20] I. Kortidis, K. Moschovis, F.A. Mahmoud, G. Kiriakidis, Thin Solid Films 518 (2009) 1208.

[21] G. Kiriakidis, K. Moschovis, I. Kortidis, V. Binas, Vacuum 86 (2012) 495.

[22] J Orloff, M. Utlaut, L. Swanson High resolution focused ion beams: FIB and its applications. Kluwer Academic/Plenum Publishers, New York (2003)

[23] N. Rowlands, P.R. Munroe Microstr Sci 26 (1998) 233.

[24] M.H.F. Overwijk, F.C. Van den Heuvel, C.W.T. Sulle-Lieuwma, J. Vac. Sci. Technol. B 11 (1993) 2021.

[25] S.J. Pearton, W.H. Heo, M. Ivill, D.P. Norton, T. Steiner, Semicond. Sci. Technol. 19 (2004) R59.

[26] J. Mera, C. Córdoba, J. Doria, A. Gómez, C. Paucar, D. Fuchs, O. Morán, Thin Solid Films 525 (2012) 13.

[27] R. Saleh, N.F. Djaja, S.P. Prakoso, Journal of Alloys and Compounds 546 (2013) 48.

[28] X.F. Liu, N. Yang, H. Li, R.H. Yu, W. Wei, Materials Letters 92 (2013) 405.

[29] A. Goktas, I.H. Mutlu, Y. Yamada, E. Celik, Journal of Alloys and Compounds 553 (2013) 259.

[30] B.D. Culity, S.R. Stock, Elements of X-ray Diffraction, Prentice Hall, New Jersey, 2001.

[31] L. Vegard, Z. Phys. 5 (1921) 17.

[32] L. Vegard, Z. Kristallogr. 67 (1928) 239.

[33] D. Toloman, A. Mesaros, A. Popa, O. Raita, T.D. Silipas, B.S. Vasile, O. Pana, L.M. Giurgiu, Journal of Alloys and Compounds 551 (2013) 502.

[34] D.E Motaung, G.H. Mhlongo, I. Kortidis, S.S Nkosi, G.F. Malgas, B.W Mwakikunga, S. Sinha-Ray, G. Kiriakidis, Applied Surface Science (2013) Accepted.

[35] S.S. Nkosi, B. Yalisi, D.E. Motaung, J. Keartland, E. Sideras-Haddad, A. Forbes, B.W. Mwakikunga, Applied Surface Science 265 (2013) 860.

[36] S.S. Nkosi, H.M. Gavi, D.E. Motaung, J. Keartland, E. Sideras-Haddad, A. Forbes, B.W. Mwakikunga, Journal of Spectroscopy, vol. 2013, Article ID 272704, 6 pages, 2013. doi:10.1155/2013/27270.

[37] V.R. Shinde, T.P. Gujar, C.D. Lokhande, R.S. Mane, Sung-Hwan Han, Mater. Chem. Phys. 96 (2006) 326.

[38] S. Banerjee, K. Rajendran, N. Gayathri, M. Sardar, V. Sengodan, Appl. Phys. Lett. 104 (2008) 043913.

[39] B.-Z. Dong, H. Hu, G.-J. Fang, X.-Z. Zhao, D.-Y. Zheng, Y.-P. Sun, J. Appl. Phys. 103 (2008) 073711.

[40] C. Song, K.W. Geng, F. Zeng, X.B. Wang, Y.X. Shen, F. Pan, Y.N. Xie, T. Liu, H.T. Zhou, Z. Fang, Phys. Rev. B 73 (2006) 024405.

[41] S.V. Bhat, P. Ganguly, T.V. Ramakrishnan, C.N.R. Rao, J. Physics C 20 (1987) 1559.

[42] V.V. Srinivasu, S.E. Lofland, S.M. Bhagat, K. Ghosh, S.D. Tyagi, J. Physics Letters 86 (1999) 1067.

[43] H. Montiel, G. Alvarez, I. Betancourt, R. Zamarano, R. Valenzuela, Appl. Phys. Lett. 86 (2005) 072503.

[44 H. Montiel, G. Alvarez, M. Gutierrez, R. Zamorano, R. Valenzuela, J. Alloys and Compounds 369 (2004) 141.

[45] F. Owens, J. Physics and Chemistry of Solids 58 (1997) 1311.

[46] H. Gavi, B.D. Ngom, A.C. Beye, A.M. Strydom, V.V. Srinivasu, M. Chaker, N. Manyala, J. Magnetism and Magnetic Materials 324 (2012) 1172.

[47] A. Veinger, A. Zabrodiskii, T. Tisnek, J. Alloys and Compounds 369 (2004) 751.

[48] R. Rakhimov, H. Ries, D. Jones, L. Glebov, Appl. Phys. Lett. 76 (2000) 751.

[49] G. Alvarez and R. Zamorano, J. Alloys and Compounds 369 (2004) 231

[50] W. Harth, R. Jaenicke,. Appl. Phys. Lett. 14 (1969) 27.

[51] T. Arizumi, T. Aoki, K. Hayakawa, J. Phys. Soc. Jpn. 23 (1967) 1251.

[52] B. Lax, J.G. Mavroides, H.J. Zeiger, R.J. Keyes, Phys. Rev. Lett. 122 (1961) 31.

[53] T. Musha, F. Lindvall, J. Hagglund, Appl. Phys. Lett. 8 (1966) 157.

[54] Shih-Wei Hung, Terry Tai-Jui Wang, Li-Wei Chu, Lih-Juann Chen, J. Physical Chemistry C 115 (2011) 15592.

[55] A. Tiwari, C. Jin, A. Kvit, D. Kumar, J.F. Muth, J. Narayan, Solid State Communication 121 (2002) 371.

FIGURE CAPTIONS AND TABLES

Table 1: Summary of the unit cell parameters (*a, c, V*, FWHM and crystallite size) of the (002) orientation for the undoped and Mn doped ZnO films deposited for 20 and 30 min.

Fig. 1: XRD patterns of the Mn doped ZnO films deposited for (a) 20 and (b) 30 min.

Fig. 2: HR-TEM micrographs of a cross sectional analyses of un-doped ZnO deposited for (a-b) 20 min, (c-d) 2 at. % Mn-doped, (e-f) un-doped ZnO deposited for 30 min and (g-h) 2 at. % Mn-doped ZnO 30 min deposited film, and their corresponding SAED patterns.

Fig. 3: EDX pattern with the composition of the elements. Elemental mapping of (c) O (d) Mn (e) Zn and (f) Ag taken from the area of the SEM as shown in (a). Elemental scan [O (green), Mn (blue), Zn (red) and Ag (purple)].

Fig. 4: AFM 3D images of (a) un-doped ZnO grown for 20 min, (b-d) Mn doped ZnO films at 0.1, 0.5 and 2 at. % deposited for 20 min, (e) undoped ZnO grown for 30 min and (f-h) Mn doped ZnO films at 0.1, 0.5 and 2 at.% deposited for 30 min.

Fig. 5: Evolution of the (a) surface roughness and (b) film thickness as a function of Mn concentration.

Fig. 6: EPR measurement for the undoped and Mn doped ZnO films deposited for 20 min. The film geometry was always kept parallel to the magnetic field and (b) corresponds to the zoom-in at low field (~ 6mT).

Fig. 7: EPR measurement for the undoped and Mn doped ZnO films deposited for 30 min. The film geometry was always kept parallel to the magnetic field and (b) corresponds to the zoom-in at low field (~ 6mT).

Fig. 8: The ΔH_{PP} dependence of FMR microwave absorption with Mn concentration measured parallel (0˚) to the magnetic flux density field for both 20 and 30 min deposited films.

Fig. 9: UV-VIS absorption spectra of the un-doped and Mn doped ZnO films deposited for (a) 20 min (b) 30 min.

Graphical Abstract

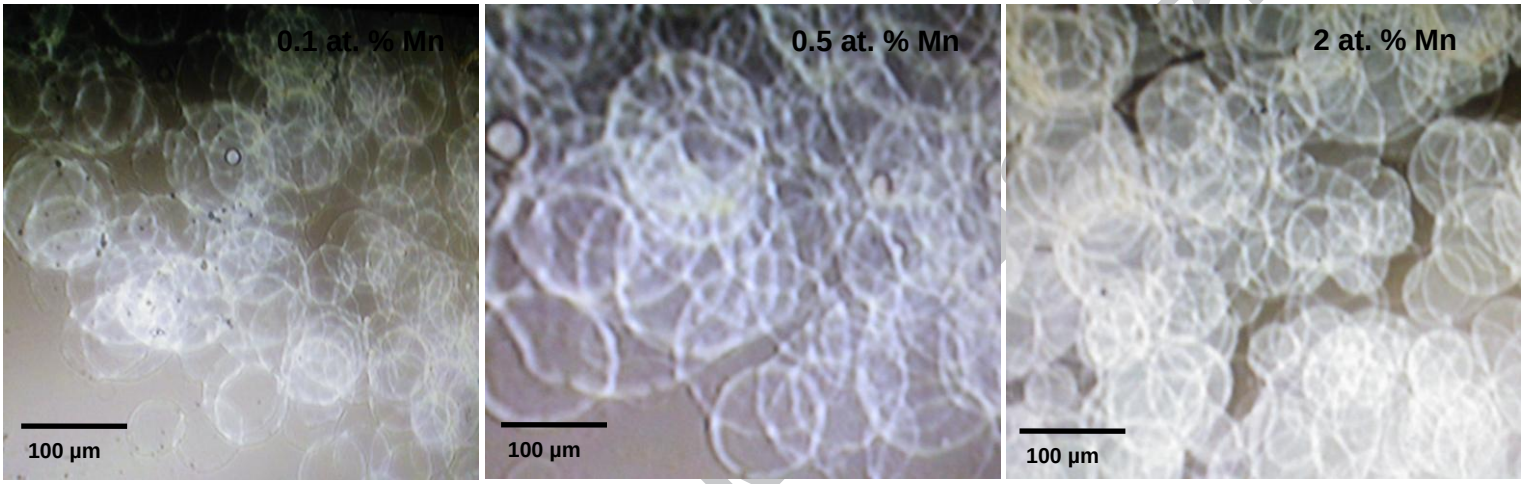

Optical microscopy images of Mn doped ZnO films deposited for 20 min

Research Highlights:

- Mn-ZnO films showing transparent spherical bubbles were synthesized by ASP.
- LFMA phenomenon was observed for these films.
- A relatively novel reversal magnetic feature to that of LFMA was observed.
- Ferromagnetic to paramagnetic transition due to Mn doping was observed.
- Angular dependence analysis showed evidence of magnetic anisotropy present.

Table 1:

Dep. Time (min)	Films	$2_{(002)}$ (°)	FWHM (°)	Crystallites size (nm)	*a* (Å)	*c* (Å)	*V* (Å^3)
20	Undoped ZnO	34.460	1.490	5.570	3.2489	5.2062	47.5895
	0.1 at.% Mn	34.501	0.347	22.881	3.2501	5.2020	47.5863
	0.5 at.% Mn	34.518	0.410	20.282	3.2549	5.1859	47.5792
	2.0 at.% Mn	34.652	2.486	3.361	3.2729	5.1710	47.9687
30	Undoped ZnO	34.453	0.290	29.090	3.2489	5.2063	47.5904
	0.1 at.% Mn	34.671	0.315	26.409	3.2501	5.1743	47.3329
	0.5 at.% Mn	34.547	0.362	22.973	3.2549	5.1940	47.6535
	2.0 at.% Mn	34.531	0.395	21.053	3.2729	5.1853	48.1013